A physical model of mantis shrimp for exploring the dynamics of ultrafast systems

Emma Steinhardt[a,1,2], Nak-seung P. Hyun[a,1], Je-sung Koh[b], Gregory Freeburn[a], Michelle H. Rosen[a], Fatma Zeynep Temel[c], S. N. Patek[d], and Robert J. Wood[a,2]

[a]John A. Paulson School of Engineering and Applied Sciences, Harvard University, Cambridge, MA 02138; [b]Department of Mechanical Engineering, Ajou University, Suwon, South Korea 16499; [c]The Robotics Institute, Carnegie Mellon University, Pittsburgh, PA 15213; and [d]Biology Department, Duke University, Durham, NC 27708

Edited by John A. Rogers, Northwestern University, Evanston, IL, and approved June 25, 2021 (received for review December 31, 2020)

Efficient and effective generation of high-acceleration movement in biology requires a process to control energy flow and amplify mechanical power from power density–limited muscle. Until recently, this ability was exclusive to ultrafast, small organisms, and this process was largely ascribed to the high mechanical power density of small elastic recoil mechanisms. In several ultrafast organisms, linkages suddenly initiate rotation when they overcenter and reverse torque; this process mediates the release of stored elastic energy and enhances the mechanical power output of extremely fast, spring-actuated systems. Here we report the discovery of linkage dynamics and geometric latching that reveals how organisms and synthetic systems generate extremely high-acceleration, short-duration movements. Through synergistic analyses of mantis shrimp strikes, a synthetic mantis shrimp robot, and a dynamic mathematical model, we discover that linkages can exhibit distinct dynamic phases that control energy transfer from stored elastic energy to ultrafast movement. These design principles are embodied in a 1.5-g mantis shrimp scale mechanism capable of striking velocities over 26 m s^{-1} in air and 5 m s^{-1} in water. The physical, mathematical, and biological datasets establish latching mechanics with four temporal phases and identify a nondimensional performance metric to analyze potential energy transfer. These temporal phases enable control of an extreme cascade of mechanical power amplification. Linkage dynamics and temporal phase characteristics are easily adjusted through linkage design in robotic and mathematical systems and provide a framework to understand the function of linkages and latches in biological systems.

ultrafast motions | linkage dynamics | bioinspired robotics | bioinspired mechanisms | mantis shrimp

Latch-mediated spring actuation (LaMSA) is a class of mechanisms that enable small organisms to achieve extremely high accelerations (1–5). Small organisms generate fast movements by storing elastic energy and mediating its release through latching. LaMSA mechanisms are found across the tree of life, including fungi, plants, and animals, with such iconic movements as found in trap-jaw ant mandibles, frog legs, chameleon tongue projection, fungal ballistospores, and exploding plant seeds (4–8). While the use of materials for elastic energy storage and release has been examined to some extent (9–11), the principles of how latches enable storage of elastic energy and mediate its release have only recently begun to be explored (12, 13). Indeed, even after half a century of investigation, one of the most extensively studied and impressive LaMSA systems, the mantis shrimp (Stomatopoda), uses a latch mechanism that is not yet fully understood.

In recent years, robots have grown in their importance as physical models for studying the mechanics and dynamics of organisms and their behaviors (14–18). Such models can be manipulated—both at design time and at run time—in ways that natural systems cannot, thus providing tools for the study of organism functional morphology, neuroethology, and operation in different environments. Here, based on previous studies of mantis shrimp biomechanics, we develop physical and analytical models to elucidate the latch-based control of energy flow during mantis shrimp strikes and, more broadly, to establish the design principles for repeated use, extreme mechanical power amplification in small engineered devices.

Mantis shrimp use a LaMSA mechanism to achieve among the fastest predatory strikes in the animal kingdom, reaching extreme accelerations with their raptorial appendages on the order of 10^6 rad s^{-2} in water. These strikes are so fast that they create cavitation bubbles and break hard molluscan shells—an impressive feat given their small size (19–22). Even the largest species, the peacock mantis shrimp (*Odontodactylus scyllarus*), has a striking appendage (carpus, propodus, and dactyl segments of the raptorial appendage, colored in purple in Fig. 1*C*) length of only 2.65 cm. Mantis shrimp store potential energy through deformation of an elastic mechanism in the merus segment which is composed of a saddle-shaped piece of the exoskeleton (the "saddle") and another stiff yet deformable region of the exoskeleton (called the "meral-V") (23–27); see the blue segments in Fig. 1*C*. These components are part of a four-bar linkage mechanism that transforms stored elastic energy into the rapid rotation of the extremely fast strikes (28, 29). Biologists have long known about two small structures, called sclerites, which are embedded in the apodemes (tendons) of the flexor muscles that release the strikes (28, 30, 31). These tiny structures

Significance

Many small organisms produce ultrafast movements by storing elastic energy and mediating its storage and rapid release through a latching mechanism. The mantis shrimp in particular imparts extreme accelerations on rotating appendages to strike their prey. Biologists have hypothesized, but not tested, that there exists a geometric latching mechanism which mediates the actuation of the appendage. Inspired by the anatomy of the mantis shrimp striking appendage, we develop a centimeter-scale robot which emulates the linkage dynamics in the mantis shrimp and study how the underlying geometric latch is able to control rapid striking motions. Our physical and analytical models could also be extended to other behaviors such as throwing or jumping in which high power over short duration is required.

Author contributions: E.S., N.P.H., J.K., M.H.R., F.Z.T., S.N.P., and R.J.W. designed research; E.S., N.P.H., and G.F. performed research; E.S., N.P.H., and R.J.W. analyzed data; and E.S., N.P.H., M.H.R., S.N.P., and R.J.W. wrote the paper.

The authors declare no competing interest.

This article is a PNAS Direct Submission.

[1]E.S. and N.P.H. contributed equally to this work.

[2]To whom correspondence may be addressed. Email: estein@g.harvard.edu or rjwood@seas.harvard.edu.

This article contains supporting information online at https://www.pnas.org/lookup/suppl/doi:10.1073/pnas.2026833118/-/DCSupplemental.

Published August 13, 2021.

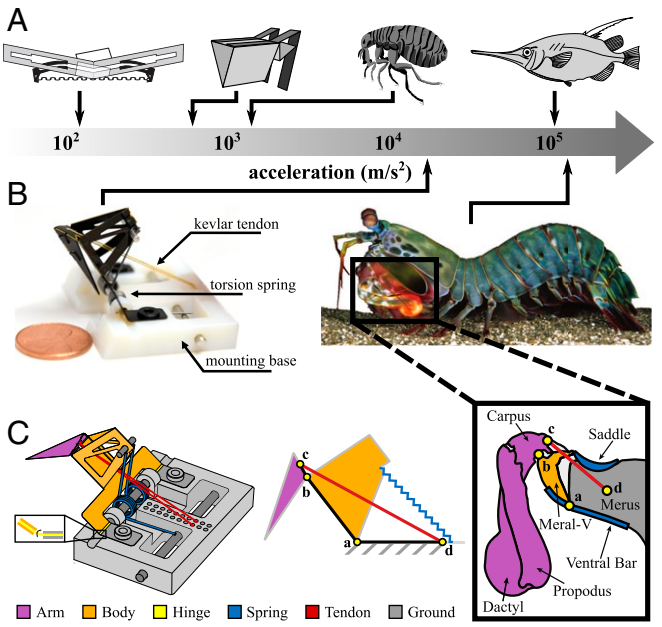

Fig. 1. An overview of biologically inspired physical models that generate extreme accelerations. (*A*) A diagram illustrating high acceleration within biological and synthetic LaMSA systems. From left to right, two synthetic systems, water strider-inspired robot (44) and flea-inspired robot (69), and two biological systems, flea (70) and snipefish (36, 71), are shown. A survey of more acceleration data of biological and synthetic LaMSA systems can be found in table 1 of ref. 4. Water strider–inspired robot image from ref. 69. Reprinted with permission from American Association for the Advancement of Science. Flea-inspired robot image ©2012 Institute of Electrical and Electronics Engineers; reprinted, with permission, from ref. 43. Flea image credit: CanStockPhoto/ottoflick. Snipefish image credit: Wikimedia Commons/Tony Ayling. (*B*) Photograph of our mantis shrimp–inspired mechanism and photograph of a peacock mantis shrimp by Roy Caldwell. The proposed mantis shrimp robot generates 10^4 m s^{-2} for striking the arm, and the mantis shrimp generates 2.5×10^5 m s^{-2} for striking the appendage (19). Photographs adjusted for contrast with background removed. Adapted with permission from ref. 28. (*C*) (*Right*) The four-bar linkage in the mantis shrimp appendage is labeled (a to d). Adapted with permission from ref. 28. The striking arm has three tightly coupled components (dactyl, propodus, and carpus), which are colored purple. Two exoskeleton elastic components are colored blue. Last, the extensor muscle, which actuates the striking motion, is colored red. (*Middle*) A geometric abstraction of the four-bar linkage with two rigid bodies, the arm and the body. (*Left*) The synthetic realization of the proposed four-bar linkage with one variable-length link. The body is highlighted orange, and the arm is purple. Flexures which allow articulation are shown in yellow. The mechanism is secured to a 3D printed base using two screws. A tendon, shown in red, is used to actuate the mechanism. A series of holes in the base allow the tendon pulling angle to be adjusted between experiments. Potential energy is stored in a torsion spring (blue).

brace against the interior of the merus segment and oppose the forces of the large, antagonistic extensor muscles that load the elastic mechanism. When the extensor muscles contract to load potential energy, the sclerites serve as a contact latch to prevent the rotation of the striking appendages. Then the flexor muscles release the sclerites to allow the striking appendage to rotate. Once the contact latch is released, the extensor muscle remains contracted while the elastic mechanism recoils to actuate the rotation of the striking body. The locked position of the sclerites and subsequent release are shown in *SI Appendix*, Fig. S13. The exact locations of the sclerites, apodemes of the flexor muscle, and meres segment in mantis shrimp can be found in figure 3 in ref. 25. A representative striking motion of a mantis shrimp can be found in Movie S5.

In general, after loading the potential energy in the spring, the role of the contact latch (sclerites) is to lock the system in this loaded configuration. For a typical spring loaded mechanism with a contact latch, and once the physical latch is removed, the spring would immediately begin to release the stored energy. However, analyses of the temporal sequence of loading and release of the strikes reveal a substantial time delay between release of these small latches and the onset of rotation of the appendage (20, 28, 32, 33). Therefore, biologists have hypothesized, but not tested, that while the sclerites initiate unlatching, a second, geometric latch mediates the actuation of the appendage by the recoiling elastic mechanism (5, 33, 34).

Latches can be classified into three types—fluidic, contact, and geometric (4, 5)—and contact latches (e.g., the sclerites shown in *SI Appendix*, Fig. S13) have previously been studied and assumed to be a primary latch mechanism in mantis shrimp. Contact latches are dependent on a physical structure blocking motion, while geometric latches are based on kinematic linkage mechanisms. Ninjabot uses a contact latch, and is, to our knowledge, the only other physical model of the mantis shrimp striking appendage (35). Ninjabot's striking arm is part of a large assembly with a hand-cranked ratchet and pawl mechanism. It was designed to emulate the speed and acceleration of mantis shrimp strikes and to characterize the fluid dynamics of the striking motion but not to emulate the linkage or latch mechanics.

Four-bar linkages can function as geometric latches if they mediate a sudden directional change of rotational motion (36–39). One type of geometric latch is a torque-reversal latch that consists of an n-bar linkage (most often a four-bar) where the kinematics of the linkage admits at least one point in the configuration space such that an infinitesimal motion of a configuration variable results in an instantaneous change in the sign of the torque around one or more joints (5). A four-bar–based geometric latch is depicted in Fig. 2 A and B in which the torque reversal is achieved when the system passes through a linkage overlap. Typically, the linkage overlap condition within a four-bar mechanism is denoted as an overcentering configuration. In engineered devices, the overcentering property of four-bar linkages is frequently used. For example, a four-bar linkage has been used to design a robust aircraft landing gear (40, 41). The spring attached within the four-bar linkage provides bistability of the down-locked and uplocked positions of the landing gear, which also reduces the load on the actuator. The primary design goal for this simple example lies in the stability of the two extreme configurations, whereas we focus our study on the rapid acceleration experienced when crossing the overcentering configuration.

Geometric latches have been proposed in fleas, snapping shrimp, and mantis shrimp (36, 38, 39, 42) and designed into synthetic systems, such as a flea-inspired insect-scale jumping robot (43). A more recent design, demonstrated in a water strider inspired robot (44), uses a symmetric four-bar torque reversal linkage (45). A four-bar linkage in snipefish feeding strikes causes a rapid rotational direction change, as inferred from functional morphology and micro-CT scans (36). Rotation reversal is initiated via a separate triggering muscle, and the four-bar linkage exhibits a singular overcentering configuration. This causes the linkage to rotate in the reverse direction after overcentering.

Until now, the mantis shrimp four-bar linkage mechanism has been analyzed solely as a mechanical pathway to transfer energy from their elastic mechanism to the rotation of their appendages (19, 28, 29, 46–49); however, through the additional lens of a hypothesized geometric latch, previous biological analyses of the linkage mechanism may need to be revisited. The four-bar linkage in a mantis shrimp's raptorial appendage is composed of four links and pivots (Fig. 1*C*) (28). The link connecting the carpus and merus is formed by contracted muscles (c–d in Fig. 1*C*) as also occurs in other biological linkage and lever mechanisms that operate as LaMSA systems only during

configurations determined by muscle activation (50–53). In mantis shrimp, the merus extensor muscles contract during spring loading and remain contracted during unlatching and spring recoil (30, 33); therefore, the link formed by the contracted extensor muscles is shorter during the operation of the LaMSA mechanism than when it is not being used (i.e., when the extensor muscles are not contracted to load the elastic mechanism) (28). The change in the extensor muscle length reduces by 10% relative to its relaxed position while loading energy in the saddle and meral-V (28).

An accurate dynamic model can allow us to explore the initiation and switching between spring loading and spring actuation phases which are crucial for control of energy flow and reducing abrupt changes that cause damage (1, 54). A previous analytical derivation of latch release dynamics for a contact-based latch model (13) was possible because the contact latch component was in contact with the projectile: the unlatched condition occurs when the latch and projectile are no longer in contact. In contrast, mathematically defining latch release for a geometric latch is challenging due to the absence of a physical component serving as a latch. Nevertheless, inspired by the fact that the mantis shrimp's striking body (carpus, propodus, and dactyl) and the meral-V are in contact while extensor muscles load the elastic components, the latching (and latched) phase can be identified by the constraint force holding the striking body and the meral-V together. As we will demonstrate in this study, a dynamic model for switching between phases can be properly defined using constrained Lagrangian mechanics (55). A dynamic mathematical model of four-bar latch dynamics has the potential to reveal previously hidden geometric latching control in four-bar systems, which is especially likely in systems with a contractile link. Thus, inspired by the controllable link length in the mantis shrimp's raptorial appendage, we construct mathematical and physical models of a mantis shrimp–inspired four-bar mechanism with three rigid links and one variable-length link (red) at c–d shown in Fig. 1*C* (akin to muscle activation control).

We take a three-pronged approach to establishing the general principles of latching dynamics in LaMSA systems and specifically the geometric latch hypothesized to control mantis shrimp striking. We first present our physical model inspired by mantis shrimp LaMSA and linkage mechanics. This physical model includes multiple degrees of freedom (DoFs) and flexure-based flexible joints and uses a linear spring for potential energy storage. In parallel, we develop a dynamic mathematical model composed of multiple rigid bodies and assume linear models for the stiffness and damping at each joint. We reanalyze and incorporate a previously published dataset of mantis shrimp kinematics to revisit the linkage dynamics and incorporate the hypothesized geometric latching process. Finally, we conduct a series of experiments on the physical model in both air and water to test how latch release can be controlled with various conditions of tendon control, fluidic loading, and mechanism design.

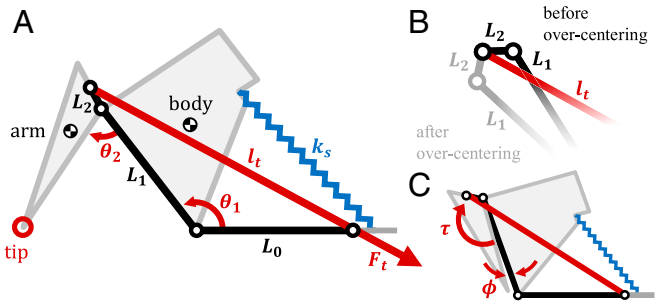

Fig. 2. A planar model for the four-bar linkage of the mantis shrimp. (*A*) Dimensions and inertial components of two rotating bodies composed with the four-bar links (L_0, L_1, L_2, l_t). Arm and body are shown. The arm rotates away from the body (θ_2) as the spring recoils (θ_1). An external force, F_t, acts on the tendon, and a torsional spring, with spring coefficient k_s, is attached between the body and ground (shown here as a linear spring for convenience; a torsional spring is used in the physical system). The two generalized coordinates are θ_1 and θ_2. (*B*) Configurations before and after overcentering are shown. The tendon links, l_t, for both configurations are colinear and thus overlap in this drawing. (*C*) Direction of the generalized constraint torque, τ, between the arm and body when in contact. The constraint torque is a reaction force which is nonzero only when the arm is in contact with the body. In our physical model, there is an offset contact angle, denoted as ϕ, between the arm and the body when they are in contact.

Results

Physical and Mathematical Models. Our mantis shrimp robot incorporates a four-bar linkage with one variable-length link at similar length scale (19 mm vs. 8 to 27 mm), appendage mass (645 mg vs. 251 mg), and striking motion as a mantis shrimp (see Table 1 for a more detailed comparison) (19, 28, 29). The design includes the four links highlighted in Fig. 1*C* with pivot points on both the robot and mantis shrimp labeled a, b, c, and d—one rigid ground link a–d (shown in gray), two more rigid links a–b and b–c (shown in black), and one variable-length link a–d (shown in red). The variable-length link is a Kevlar tendon that connects the actuator (linear motor) to the four-bar linkage. The tendon is free to rotate at the connection to the four-bar and is kept in tension during the loading phase. We fabricated the device (Fig. 1) using a multiscale, multimaterial process [pop-up book MEMS (microelectromechanical systems) (56, 57)] where rotary joints in the four-bar linkage are approximated using compliant flexures. A densely woven Kevlar fabric is laminated with polyimide to reinforce the typically polyimide-only flexures to increase robustness and reduce flexure tearing. The laminate structure is folded and held in place with cyanoacrylic glue to form a three-dimensional (3D) structure. A torsion spring is incorporated between the ground link and the first rigid link. In order to keep the axis of the spring in line with the rotational axis of the flexure, the body is mounted on a 3D printed base. One end of the torsion spring is fixed to the base while the other is free to move against the body. A strand of Kevlar, used as the tendon, is tied to the arm, and its angle in relation to the body can be adjusted by guiding it through various holes in the 3D printed base.

One of our goals for the design and manufacturing of our physical model is to match the scale of real mantis shrimp (Table 1) since inertial, fluidic, and elastic forces scale at different rates (58). By being faithful to the (approximate) scale of real mantis shrimp, our at-scale physical model can help probe the contributions of the features of the geometric latching mechanism and test theories postulated by biologists about the role of internal and external forces (28).

A constrained Lagrangian mechanics mathematical modeling approach successfully identifies the causal basis for the latched–unlatched transition in LaMSA mechanisms in general and the geometric latching mechanism specifically in the physical model and mantis shrimp. This dynamic model is a simplification of the physical model such that the mathematical model operates in one plane with two rigid bodies (arm and body; Fig. 2*A*) connected by a single revolute joint. Two generalized coordinates, $q = (\theta_1, \theta_2)$, are chosen to derive the equations of motion where the L_0 link is fixed to the mounting base.

The kinematics of the four-bar in the physical model are incorporated into the mathematical model of the dynamics. The planar model in Fig. 2*A* shows a four-bar linkage consisting of three rigid links (L_0, L_1, $andL_2$) and one variable-length link, l_t. The system is solely actuated by the force, F_t, pulling the Kevlar

tendon along the link l_t. As the tendon is pulled, l_t decreases, and the configuration of the four-bar linkage changes accordingly. A sequence of four-bar linkage configurations is shown in Fig. 3*C*. An animation of the four-bar linkage kinematics can be found in Movie S4, which visualizes the full motion from loading to arm release.

The dynamics of the system are modeled using Lagrangian mechanics with a holonomic constraint on the generalized coordinates (55). The holonomic constraint prevents penetration between the arm and the body when the two parts are in contact as shown in Fig. 2*C*. This constraint is only active when θ_2 reaches a specific angular offset, $\phi \geq 0$, that describes the contact between the two components (Fig. 2*C*). If the constraint force is active, thus making the arm remain in contact with the body, the number of DoFs is reduced to one. Therefore, the full dynamics of the system switches between two modes where one is fully actuated (1 DoF with a single control) and the other is underactuated (2 DoFs with a single control). The dynamics of the system are then derived as

$$M(q)\ddot{q} + C(q,\dot{q})\dot{q} + G(q) = F_{\mathrm{d}}(q,\dot{q}) + B(q)F_t + e_2\lambda(q,\dot{q}), \quad [1]$$

$$\lambda(q,\dot{q}) = \begin{cases} \tau(q,\dot{q},F_t) & if\theta_2 = \phi and \tau(q,\dot{q}) \geq 0 \\ 0 & \text{otherwise} \end{cases}, \quad [2]$$

where $e_2 = (0,1)^T$, $M(q) \in \mathbb{R}^{2\times 2}$ is the inertia matrix, $C(q,\dot{q})$ is the Coriolis matrix, $G(q) \in \mathbb{R}^2$ contains conservative forces (gravity and spring forces), $F_{\mathrm{d}}(q,\dot{q}) \in \mathbb{R}^2$ contains all other nonconservative forces (e.g., torsional damping on the joints, fluidic drag), $F_t > 0$ represents the pulling force from the Kevlar tendon, $B(q)F_t \in \mathbb{R}^2$ is the generalized actuator force, and $\tau(q,\dot{q},F_t)$ represents the generalized constraint force to avoid penetration when the two bodies are in contact (*SI Appendix, Mathematical Modeling*). The constraint torque $\lambda(q,\dot{q})$ is always nonnegative as the arm and the body only push against each other as shown in Fig. 2*C*.

The four-bar linkage with a variable-length link provides a way to latch the arm to the body while loading energy into the spring. The variable link length introduces an extra degree of freedom which is used to keep the system latched while loading the spring; this cannot be achieved if all links are fixed in length. By pulling the tendon, the length l_t is reduced, which results in an overlap between the L_2 and l_t links.

A configuration where the links L_2 and l_t overlap is denoted an overcentering configuration. Prior to overcentering, the tendon is below the θ_2 pivot (joining links L_1 and L_2), and after overcentering it is above the pivot (Fig. 2*B*). Since the proposed four-bar linkage has two DoFs (i.e., when the arm and body are separated), there exists an overcentering configuration for every θ_1. Since a smaller θ_1 results in greater potential energy in the spring, different spring energy levels are achievable by choice of θ_1 at overcentering.

LaMSA Phases and Latching Dynamics. Our mathematical model reveals four temporal phases based on the linkage and spring dynamics and the actuation input. These phases illuminate three new aspects of LaMSA in linkage systems: 1) a separation between the unlatching event and the overcentering configuration, 2) extended potential energy loading after overcentering, and 3) a generalized notion of system being latched without a contact latch component. During phase I, the model begins in a locked configuration with the arm and body in contact, and initial actuation contracts the spring to store potential energy (Fig. 3*C*). Phase II begins when the arm and the body separate, introducing a second degree of freedom. Phase III begins when the system reaches the overcentering configuration and the arm angle (θ_1) and body angle (θ_2) accelerate rapidly. During phases I through III, the spring is loaded with potential energy until it reaches a maximum. The fastest arm motion is achieved in phase IV when elastic potential energy is converted to kinetic energy of the arm rotation (Fig. 3*A*). An animation of the four phases can be found in Movie S4.

These four temporal phases are categorized into latched (phase I) and unlatched (phases II to IV). The mathematical model represents the latched mode when the constraint in Eq. **2** is active, meaning that the arm and the body are in contact and pushing against each other (Fig. 2*C*). In contrast, the unlatched mode occurs when the constraint in Eq. **2** is inactive, meaning that the arm and the body either are not in contact or are in contact but not pushing against each other. This mathematical representation of latched and unlatched conditions thereby defines latching as a dynamic phenomenon, without identifying any specific component as being a latch.

In our modeled system, regardless of the latch type (geometric or contact), the latched to unlatched transition can be dynamically changed by the input force generated by pulling the tendon. Therefore, there are two objectives of the actuation mechanism (pulling the Kevlar string, for the physical model). One is to load potential energy in the spring while latched, and the other is to trigger the transition from the latched to the unlatched configuration. In addition, switching from the latched to unlatched condition depends on the input force and the configuration of the whole system (*SI Appendix, Latched Mode Switching* and Fig. S1).

These same latch dynamics and four temporal phases are present during the operation of our physical model. In phase I (Fig. 3 *A* and *C*), the arm and body move together with the arm rotating around the θ_1 pivot. The angular velocity of the arm (with respect to the body), $\dot{\theta}_2$, is nearly zero (up to numerical precision) during this phase while the spring is contracting, and $\dot{\theta}_1$ stays negative (Fig. 3*B*). The model predicts that phase I ends when the system becomes unlatched, and the arm will rotate away from the body (i.e., an increase in θ_2) after phase I. The kinematic data from our experiments verify the increased arm velocity, $\dot{\theta}_2$, by crossing over from phase I to phase II (Fig. 3*B*).

During phase II, the spring continues to load more potential energy as $\dot{\theta}_1$ is negative, and the arm begins to separate from the body, increasing the generalized coordinate θ_2 and approaching the overcentering condition. Video frames in Fig. 3*A* verify the arm departing from contact in phase II, and Fig. 3*B* shows an increase in the angular velocity of the arm, $\dot{\theta}_2$. Phase II ends when the system becomes overcentered, which serves as a key indicator of the transition between phases (i.e., a switch from low acceleration to high acceleration) in the unlatched configuration. The model predicts that the tendon force decelerates arm rotation in phase II, whereas this force accelerates arm rotation in phase III (*SI Appendix, Geometric Conditions for Over-Centering*). The difference in the robot's arm acceleration between phases II and III is evident through an abrupt change in slope before and after overcentering (zoomed-in window of $\dot{\theta}_2$; Fig. 3*B*).

Phase III begins after overcentering and ends with the maximum spring contraction when the angular velocity of the body, $\dot{\theta}_1$, reaches zero. Phase III's duration (66 ms) is an order of magnitude shorter than prior phases (phase I, 1.0 s; phase II, 0.8 s) due to the high accelerations of the arm and body (Fig. 3*B*). In this short period of time, the spring is still contracting due to the inertia of the system.

Spring contraction during phase III is also observed in our reanalysis of previously published mantis shrimp strikes (33) (Fig. 3*E*). The derivative of the angle between the meral-V and the merus was used to estimate $\dot{\theta}_1$. Similarly, the derivative of the angle between the propodus and meral-V represents $\dot{\theta}_2$. The

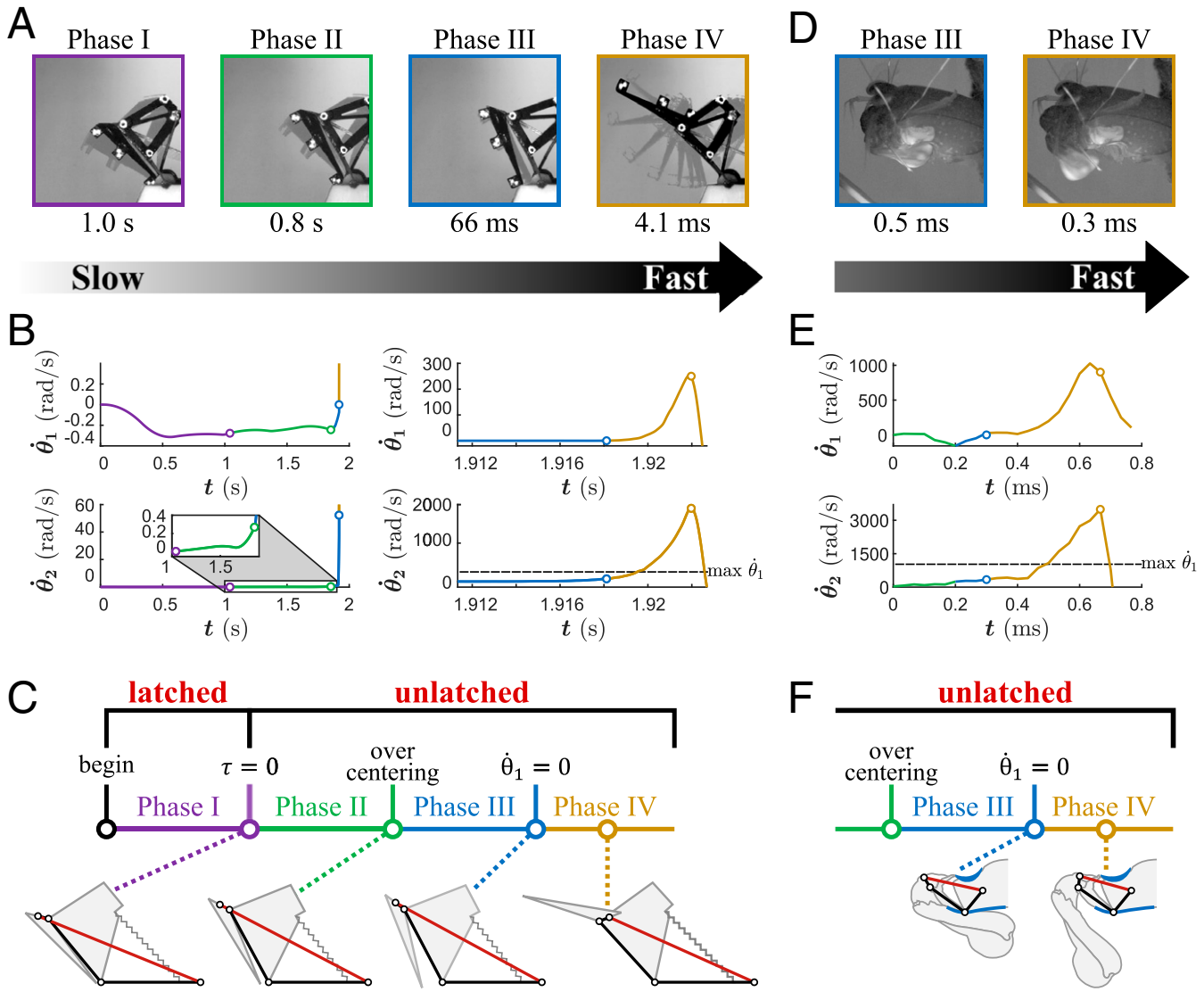

Fig. 3. Temporal phase transition diagrams with representative experimental data and a comparison with biological data from mantis shrimp strikes presented in ref. 33. (*A–C*) Experimental data of the motion of the physical model, with a controlled tendon pulling speed of 2.3 mm s^{-1} in air (*Materials and Methods*). (*D–F*) Two fast phases (phase III and phase IV) of a mantis shrimp strike (from ref. 33) are shown. (*A*) Snapshots of the experiments for each phase are overlaid with shadows. The last snapshot images at the end of the phase (before switching to the next phase) are displayed with a darker color. The full motion video can be found in Movie S1. (*B*) The filtered rotational velocities (*Data Processing*) of the generalized coordinate for the slow phases (phases I and II) (*Left*) and the fast phases (phases III and IV) (*Right*). Slow phase data in *Left* was additionally spline fitted using a free-knot spline approximation. (*C*) The temporal phases with representative kinematic diagrams corresponding to the video frames in *A*. The purple, green, blue, and brown colors represent phases I, II, III, and IV, respectively. (*D*) Snapshots of the mantis shrimp striking motion. (*E*) Filtered rotational velocity of the coordinates defined in ref. 33. (*F*) A geometric depiction based on the video frames in *D* of the appendage configuration of the mantis shrimp during phases III and IV with approximate linkage configurations. Adapted with permission from ref. 28.

striking motion includes a nonnegligible time window when $\dot{\theta}_2$ is positive while $\dot{\theta}_1$ is negative (Fig. 3*E*). Therefore, the mantis shrimp's meral-V or saddle is still contracting after the initiation of the striking motion, which implies the existence of phase III. To our knowledge this additional spring loading has not previously been documented in kinematic analyses, yet is key to how mantis shrimp unlatch their strike mechanism and is consistent with electromyography analyses (30, 33).

Returning to our analysis of the robot's strike, phase IV (strike phase) encompasses the highest arm rotational velocity when it is driven by stored elastic potential energy. The arm reaches its maximum angular velocity within a few milliseconds (4.1 ms [Fig. 3]). The arm's peak velocity ($\dot{\theta}_2$) is nearly six times faster than the peak rotational velocity of the body (Fig. 3*B*). Similarly, the mantis shrimp strike in Fig. 3*E* shows that the propodus' peak velocity ($\dot{\theta}_2$) is nearly three times higher than peak rotational body velocity ($\dot{\theta}_1$).

A notable time delay between the release of the sclerites and the extension of the saddle (release of the spring energy) has been reported in several species of mantis shrimp: 0.9 ± 0.5 ms for *O. scyllarus* and ~0.7 ms for *Neogonodactylus bredini* (28, 33). During this time period, the propodus rotates ~5° (cf. 55° at the impact), while the saddle only extends ~0.08 mm out of a total contracted displacement 2 mm for *O. scyllarus* (28). These two species are similar in scale to our robot in terms of the striking arm length and mass as reported in Table 1. Even though our proposed four-bar linkage system simplifies the degrees of freedom relative to actual mantis shrimp, we observe two phases

(phase II and phase III) where the arm loses contact with the body and starts rotating (i.e., unlatched) while the spring has not yet been released. We postulate that the behavior in phases II and III occurs after the release of the sclerites since the arm starts to rotate slowly. Similar to actual mantis shrimp motion, there is significant time spent in these phases in our physical model—0.8 s for phase II and 66 ms for phase III while the arm rotates 12°, as shown in Fig. 3*A*—before the release of the spring energy. Although the time durations of phases II and III are longer than the reported time delay in mantis shrimp, the existence of phases II and III in our proposed mechanism supports the hypothesis of the presence of a geometric latching mechanism in mantis shrimp, as speculated by biologists in refs. 5, 33, and 34.

Performance and Robustness of Mantis Shrimp Robot. The mantis shrimp robot not only emulates the extraordinary mechanics and kinematics of live mantis shrimp, it also serves as a powerful test system for establishing the robustness, performance, and metrics for performance in LaMSA mechanisms through simple manipulation of tendon control via different pull rates, environmental loading (i.e., water vs. air), and design changes (e.g., joint-to-tendon length).

The robot's linkage mechanism allows it to dynamically load different potential energy levels and traverse different dynamic regimes which results in switching from latched to unlatched at different spring potential energy levels. The switch from latched to unlatched is dynamically constrained and depends not only on the input tendon force (related to the tendon pulling rate and the configuration of the system, including the contact angle [ϕ]) and the joint-to-tendon length (L_0), both defined in Fig. 2*C* (*SI Appendix*, *Contact Force*).

Throughout our experiments, with various values for ϕ and L_0, four aspects of our physical model were studied: 1) the capability of loading potential energy to different levels, 2) the correlation between the maximum potential energy and two performance metrics (i.e., the maximum tip velocity and the kinetic energy distribution between the arm and the body), 3) performance changes under different loading conditions (i.e., in water vs. in air), and 4) a comparison between the work done by the input and the released potential energy during the fast phase (phase IV).

The maximum spring potential energy (PE_{max}) can be controlled via by multiple pathways. Higher values of PE_{max} (above 105 mJ) among the $L_0 = 23$ mm (in air) group were achieved when the contact angle ϕ was relatively small (less than 6.0°). Since the contact angle ϕ for 32 experiments with $L_0 = 23$ mm in air are not directly controlled, an additional seven tests with a set of fixed contact angles by attaching a thin shim (Movie S3 and *Materials and Methods*) were performed (Fig. 4*C*). A positive correlation between PE_{max} and the contact angle ϕ, with $R^2 = 0.983$, is verified in Fig. 4*C*. The correlation between the maximum elastic potential energy and the contact angle ϕ is also predicted in the analytical switching constraint [**2**] (*SI Appendix*, *Latch Mode Switching*). Having a larger contact angle ϕ shifts the upper bound of the switching surface to the right in *SI Appendix*, Fig. S1*C*, which causes the system to be unlatched at a larger angle θ_1 (smaller potential energy) with the same level of input force.

The maximum potential energy is also related to the overcentering configuration (Fig. 4*B*). When overcentering occurs at a lower potential energy (i.e., larger θ_1), less potential energy is stored, which corresponds to a smaller PE_{max}. However, higher potential energy at overcentering is not always correlated with a higher maximum potential energy as there are some trajectories which intersect each other during phases III and IV (Fig. 4*B*): phase III dynamics are both a function of the arm and body configuration and a function of their movement (velocity) during overcentering. Therefore, maximum loading can be achieved differently based on the motion at overcentering.

Our mathematical modeling suggests that a shorter joint-to-tendon length, L_0, allows for greater maximum potential energy; experiments with our physical model support this prediction. The analytical condition for overcentering predicts that a shorter L_0 directly results in lower θ_1 overcentering positions when in contact, which suggests higher loaded potential energy at overcentering (Fig. 4*E*). By considering the correlation between the maximum potential energy and the overcentering configuration, higher maximum potential energy is expected for the $L_0 = 19$ mm group compared to the $L_0 = 23$ mm group in experiments in air (Fig. 4*A*).

Performance Analysis. The tip velocity (red circle in Fig. 2*A*) and the ratio of arm kinetic energy to total kinetic energy (KE_2/KE) are the two performance metrics we use to evaluate our robot. The highest tip velocity recorded among 32 tendon control experiments in air with $L_0 = 23\ mm$ is ~30 m s^{-1} (Fig. 5*A*). A faster maximum tip velocity (above 26 m s^{-1}) is achieved by relatively larger maximum potential energies (above 105 mJ) among experiments in air with L_0 =23 mm. Additionally, the measured force exerted on the system during phase IV is not significantly higher in the experiments which attain higher maximum potential energies (Fig. 5*C*).

The second metric, KE_2/KE, quantifies the degree to which the spring potential energy is transferred to the arm rotational motion. If the arm kinetic energy ratio is above 0.5, then the released potential energy is transferred to a greater extent to the arm than to the body. The trajectories with PE_{max} greater than 105 mJ in Fig. 5*D* show that the arm kinetic energy ratio stays above 0.5 throughout the entire duration of phase IV. Storing more energy in the spring yields greater tip velocity and greater distribution of potential energy to the arm than the body (Fig. 5 *A* and *B*).

The robot's dynamic behavior and performance in air is congruent with its behavior in water with some key differences related to strike velocity, output variability, and sensitivity to varying inputs. The four phases and overcentering behavior also occur in water. The primary differences between water and air occur during the fast phase due to the hydrodynamic effects of velocity-dependent drag and the added mass effect from entrained fluid around the arm. When operating in water, the robot rotates 20% more slowly than in air when operated at the 2.3 m/s tendon rate (*SI Appendix*, Fig. S2*C* and Movie S2). Even so, these slower strikes in water yield a more stereotyped output with less sensitivity to varying potential energy levels (Fig. 5*A*).

In contrast to experiments in air, there is more kinetic energy in the arm than the body throughout all water experiments during phase IV, regardless of the tendon pulling velocity (Fig. 5*F*). One likely explanation is the added mass effect for the arm during phase IV as the arm rotational speed ($\dot{\theta}_2$= 290 rad s^{-1}) is roughly 10 times greater than that of the body ($\dot{\theta}_1$= 31 rad s^{-1}) as shown in *SI Appendix*, Fig. S2*C*. Another possibility is that the fluidic drag and added mass effect on the body delay the release of the spring. We observe that less than 20% of the maximum potential energy is released during phase IV (Fig. 5*F*). Since the spring and body are constrained to each other, the delay in the spring release results in less kinetic energy of the body. Furthermore, greater maximum potential energy is required in air to achieve a kinetic energy ratio greater than 0.7, compared to the case in water (Fig. 5*B*).

Released Potential Energy and Work Done by the Input. The LaMSA mechanism provides a way to overcome the limits inherent in muscle by utilizing stored potential energy and rapid spring recoil to actuate the strike. To verify this, we analyze how the

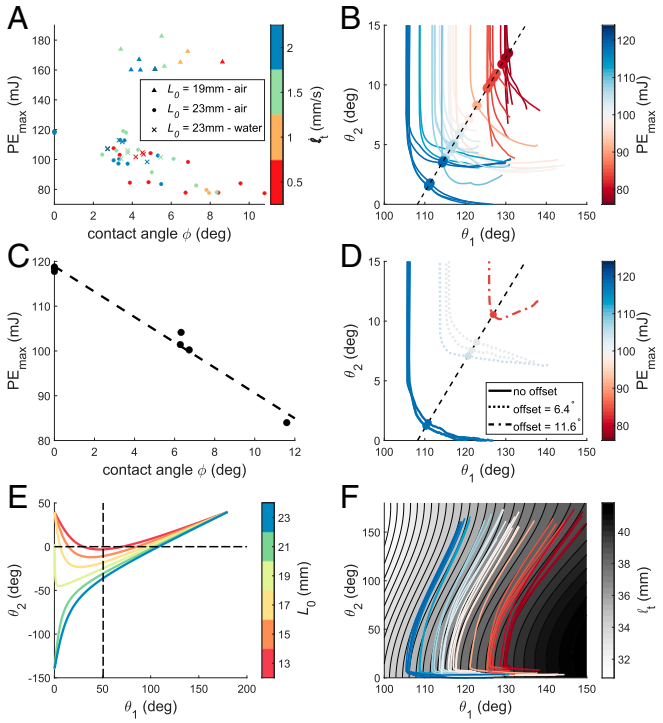

Fig. 4. Various potential energy levels achieved by different tendon pulling speeds ($\dot{l}_t$), contact angles (ϕ), and joint-to-tendon lengths (L_0). The spring potential energy is calculated based on a linear torsional spring model with the measured θ_1 angle data (*SI Appendix, Simulation and System Identification*). Higher maximum loaded potential energy, PE_{max}, can be achieved by reducing the contact angle, ϕ, and joint-to-tendon length, L_0. Also, a higher loaded potential energy at the overcentering position tends to attain a higher PE_{max}. (*A*) The relationship between PE_{max} and the contact angle ϕ for different pulling speeds $\dot{l}_t$ are shown, with the pulling speed color coded. The circles and crosses represent the $L_0 = 23$ mm tests in air and water, respectively. The triangles represents the $L_0 = 19$ mm tests in air. (*B*) Trajectories for phases II, III, and IV are shown in the (θ_1, θ_2) space for $L_0 = 23$ mm group (in air). The circle represents the overcentering position. The trajectories below the dashed black line represent phases I and II, and the trajectories above the dashed line correspond to phases III and IV. After overcentering, the system continues to load more potential energy (reducing θ_1), while the arm starts to rapidly rotate (increasing θ_2). (*C*) Controlled contact angle tests with $\phi = 0, 6.4°$, and $11.4°$ showing the correlation between PE_{max} and contact angle. The tendon pulling speeds for all seven tests are regulated to 2.3 mm s^{-1}. (*D*) Same as *B* but for the controlled contact angle experiments. (*E*) Analytical overcentering configurations for varying joint-to-tendon lengths, L_0, showing that different overcentering configurations can be achieved based on different values of L_0 (*SI Appendix, Geometric Conditions for Over-Centering*). Two reference lines show the physical limits of the system. The reference line at $\theta_2 = 0°$ represents contact of the arm and body. The second reference line represents when the body touches the base. (*F*) Full trajectories of experiments with the $L_0 = 23$ mm group (in air) are projected on (θ_1, θ_2). Each trajectory starts from a small θ_2 value and a large θ_1. The same color map as in *B* is used to represent PE_{max}. The surface of tendon lengths, $l_t(q)$, vs. the generalized coordinates is color coded (black to white). The black contour lines represent the level sets of $l_t(q)$, and the tendon lengths along the black contours remain constant. As the tendon is pulled, the tendon length is reduced and makes a sharp turn near the maximum spring contraction (i.e., minimum θ_1).

impulsive motion is achieved by spring recoil rather than by the work done from the tendon during the fast phase (phase IV). It is very difficult to stimulate the extensor muscles independently to measure the input force generated by the muscles in mantis shrimp (23, 24). Instead, the force displacement properties of the elastic material in the exoskeleton can be measured by mechanically deforming a single appendage while connected to a load cell to find the maximum force and work done by the spring (the saddle and the meral-V) (23, 24). A typical range of maximum forces measured from the exoskeleton of *Gonodactylus smithii* species are reported as 39.8 ± 10.7 N as shown in table 2 of ref. 30. Interestingly, as the power of the extensor muscle is limited at these small scales, the mantis shrimp contracts the saddle and meral-V by only a small amount (less than 1 mm), which loads 16.8 ± 6.3 mJ to the exoskeleton as reported in table 2 and figure 3 of ref. 30.

One of the benefits of our proposed physical model is to overcome challenges and limitations in the study of the functional morphology of natural systems (e.g., the difficulty in measuring the input force generated by the extensor muscle). The physical model allows us to directly measure the input force, as shown in *SI Appendix*, Fig. S12*C*. The work done by the tendon and the loaded potential energy in this experiment (the same as the one used in the kinematic analysis in Fig. 3*B*) are shown in *SI Appendix*, Fig. S12 *A* and *B*, where the net potential energy loaded during the experiment is computed to be 35.9 mJ. The displacement of the tendon in the experiment was 3.7 mm (where $l_t = 41$ mm at the beginning of phase I)—greater than the displacement of the exoskeleton in mantis shrimp. However, the stored potential energy is in a similar range, which indicates that the torsional spring used in the physical model is less stiff than the elastic material in mantis shrimp.

Nevertheless, the physical model can be used to justify the high power delivery of the geometric LaMSA mechanism by comparing the release of the potential energy with the work done by the tendon input during the spring release phase (phase IV). In our experiment, the work done by the tendon during phase IV is 0.76 mJ while the amount of the potential energy released is 23.6 mJ (the potential energy difference between the start of phase IV and the moment tip velocity reached maximum). The trajectories of experiments in air during phase IV, aligned with the level set of the tendon length map, also support the notion that the change of tendon length in phase IV is relatively small (Fig. 4*F*). Therefore, the extremely high acceleration observed in the kinematic data in Fig. 3*B* is driven by the impulsive release of the spring energy, which verifies the effectiveness of geometric latching mechanisms for the generation of high acceleration.

Sensitivity Analysis for Different Robot Geometries. The analytic switching condition from latched to unlatched in Eq. **2** shows that switching depends on internal parameters such as the center of mass and the size of the robot (L_1 and L_2) and external parameters such as different L_0 values and contact angles between the arm and the body (*SI Appendix, Contact Force*). Here we consider two external geometric parameters of the robot: the joint-to-tendon length, L_0, and the contact angle, ϕ.

Both the tip velocity and kinetic energy ratio metrics are affected by the change in the joint-to-tendon length. First, a longer L_0 provides a lower maximum potential energy required to achieve a similar average maximum tip velocity and a higher SD for maximum tip velocity (Fig. 5*A* and *Materials and Methods*). Therefore, a longer L_0 is more energy efficient and also provides a greater range of maximum tip velocities by mediating the spring actuation. On the other hand, a shorter L_0 results in a higher kinetic energy ratio relative to the maximum tip velocity (Fig. 5*B*). Similar to the results from experiments in water, less than 20% of PE_{max} is released during phase IV (Fig. 5*H*). Since PE_{max} is higher for a shorter L_0 (Fig. 5*A*), a smaller portion of the maximum potential energy was sufficient to transfer the energy to the arm without rotating the body excessively. This results in lower kinetic energy of the body during phase IV and a greater kinetic energy ratio of the arm for the shorter L_0 case.

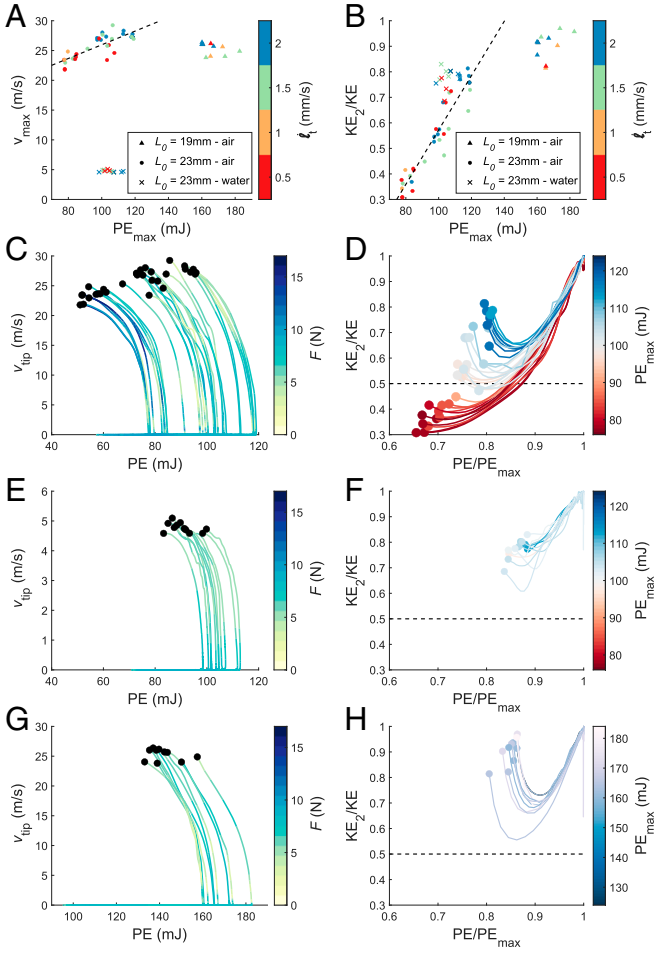

Fig. 5. Analysis of the maximum tip velocity and kinetic energy distribution during phase IV for different loading conditions (i.e., air and water) and different values of L_0. (*A* and *B*) The relationship between the two performance metrics and the maximum loaded potential energy, PE_{max}, is shown. Greater maximum loaded potential energy, PE_{max}, leads to higher performance for experiments in air with $L_0 =$ 23 mm. (*C–H*) The trajectory of the maximum tip velocity and the kinetic energy distribution during phase IV versus the potential energy. The value PE/PE_{max} describes the normalized potential energy. The filled circles represent the moment of maximum tip velocity. (*A*) A linear regression using the minimum mean squared error for experiments in air with $L_0 = 23$ mm is shown as a dashed line with $R^2 = 0.6436$. Among the $L_0 = 23$ mm group, the SD (from trial to trial) is significantly reduced in water (0.17 m s^{-1}) compared to air (2.04 m s^{-1}). (*B*) A linear regression using the minimum mean squared error for experiments in air with $L_0 = 23$ mm is shown as a dashed line with $R^2 = 0.8865$. (*C*) The applied force (color coded) over the course of the trajectory was less than 18 N. During the slow motions in phases I and II, the tip velocity remains nearly zero while the spring potential energy increases. Once the maximum potential energy is reached, the tip velocity rapidly increases and reaches its maximum (black circles). (*D*) Phase IV arm kinetic energy ratio vs. normalized potential energy for 32 experiments (in air with L_0=23 mm). Phase IV starts at unity for both axes (*Materials and Methods*). During phase IV, the spring releases potential energy, which results in a decrease of PE/PE_{max}. Potential energy is converted to kinetic energy of the arm and the body, where the KE_2/KE metric shows how the kinetic energy is distributed between the arm and the body. The color scheme is based on PE_{max}. (*E* and *F*) Similar to the experiments in *C* and *D* but in water. The added mass effect is considered in the calculation of the kinetic energy (*Materials and Methods*). The fluidic loading in water causes the arm to rotate slower compare to experiments in air, but distributing more kinetic energy to the arm. (*G* and *H*) Similar to the experiments in air in *C* and *D* but with $L_0 = 19$ mm. A shorter L_0 leads to load more potential energy, but the maximum tip velocity is not substantially increased. However, the potential energy was distributed to a greater extent to the arm compared with the experiments with a longer L_0.

The sensitivity analysis reveals some interesting trends in the design space that can alter the latching behavior of the system. For example, a shorter L_0 makes our geometric latching mechanism more stereotyped as the maximum tip velocity is not affected by how much energy is loaded in the spring and the arm tends to have more kinetic energy than the body. On the other hand, a longer L_0 provides a way to generate a range of maximum tip velocities by controlling the contact angle ϕ (*SI Appendix*, Fig. S11 *B* and *C*).

Discussion

Through a physical model, empirical experimentation with the physical model in different environmental and loading conditions, dynamic mathematical modeling, and analysis of a biological dataset, we establish the quantitative principles of the phases of LaMSA and latching, demonstrate a linkage-spring based approach to LaMSA robots, and offer a lens on the function of four-bar linkages in biology. The fast motion and temporal asymmetries of the mantis shrimp raptorial appendage are captured with our analytical model and our physical latching and linkage mechanism. Four distinct temporal phases (Fig. 3) of the striking motion are defined, extending the traditional LaMSA temporal phases (4, 5) to incorporate phases defined within the dynamics of this system. These phases illuminate how the system is unlatched prior to overcentering, leading to an intermediate period between unlatching and overcentering that has not been previously described in these systems (5, 44) and is likely a crucial feature enabling repeated and extreme use without the wear and tear of contact latching mechanisms.

Our physical model of the mantis shrimp striking mechanism is an at-scale physical model that emulates the linkage mechanics of mantis shrimp and achieves ultrafast motions. The striking acceleration of our physical model in air reached 5.7×10^4 m s^{-2} (the striking arm length multiplied by the angular acceleration in Table 1) which exceeds the performance of other small-scale (less than 14 cm) LaMSA-based engineered devices tested in air ($< 10^3$ m s^{-2}) as reported in ref. 4. We applied multiscale manufacturing methods and a detailed dynamical model that captures the fast, nonlinear, and aperiodic behavior of both the biological and synthetic systems. Additionally, our model is able to operate as a LaMSA mechanism and as a directly actuated system for slower, manipulative movements, much like mantis shrimp which can move their raptorial appendages directly through muscle contraction and can switch to operating LaMSA; in both the physical model and biological system this ability to move directly with the motor and/or via spring actuation is possible because of the presence of a variable length link in the four-bar mechanism. In addition, the ability to operate the robot in both air and water allowed us to experimentally demonstrate the significance of loading on the operation of LaMSA mechanisms. Two specific key findings include 1) the reduced variability of striking velocity in water and 2) the drag and added mass effect on the body caused a delay in unlatching, resulting in less kinetic energy in the body. The effect of load impedance on LaMSA performance is an area ripe for future investigation (44, 59).

Although the striking acceleration of the robot in air exceeds other similar at-scale engineered devices reported in ref. 4, the striking acceleration in water (10^4 rad s^{-2}) is still less than the striking acceleration of the mantis shrimp (up to 10^6 rad s^{-2}). Possible future directions to increase accelerations in water may involve optimization of the four-bar linkage design and exploration of various springs, such as a buckling spring which is geometrically similar to the saddle in the mantis shrimp.

The control of impulsive energy flow through geometry is a rich area for both mathematical analysis and materials research (60), and here we broaden that field to incorporate the role of geometry and linkages in the latching and unlatching of extreme

Table 1. Size, linear and rotational velocities, rotational acceleration, and mass comparison of three smashing mantis shrimp species, *N. bredini* (33, 47, 72), *O. scyllarus* (20, 47), and *G. smithii* (19, 29, 35); Ninjabot (35); and our mechanism

Species/robot	Striking arm (mm)	Link a–b (mm)	Link b–c (mm)	Fluid	Tip velocity (m/s)	Angular velocity (rad/s)	Angular acceleration (rad/s^2)	Mass (g)
N. bredini	8.7 ± 1.6	3.2	0.5	Water	11.3 ± 4.9	$1{,}585 \pm 755$	5.8×10^6	1.6 ± 0.6
O. scyllarus	26.5 ± 3.6	10	1.6	Water	14 ± 1.8	605 ± 51	9.4×10^5	46.7 ± 16
G. smithii	8.2 ± 2.5	4.4 ± 0.4	0.6 ± 0.1	Water	20.2 ± 4.1	$2{,}821 \pm 6{,}82$	1.1×10^7	5.4 ± 0.9
	37.1			Water	8.5 ± 5.5	$229 \pm 1{,}48$	4.2×10^5	
Ninjabot*	51.4	N/A†	N/A†	Water	10.7 ± 4	207 ± 75	3.3×10^5	9,000
	68.9			Water	18 ± 4.3	262 ± 62	3.7×10^5	
Our robot	18.7	19.1	1.5	Water	4.8 ± 0.2	307 ± 16	4.4×10^4	1.5‡
Our robot	18.7	19.1	1.5	Air	25.7 ± 2.0	$1{,}863 \pm 78$	1.3×10^6	1.5‡

*Data reanalyzed.
†Not applicable; Ninjabot does not contain a four-bar linkage.
‡Mass without base; with base 12.8 g.

dynamical systems. The four-phase temporal categorization for geometric latching behavior supports the discovery of a phase when the system is unlatched (i.e., arm movement is initiated) before overcentering occurs. The existence of such a phase was not recognized in previous studies of geometric latches which only focused on the kinematics before and after overcentering (28, 36). These four phases are essential for explaining the control of energy flow during mantis shrimp strikes and for building repeated-use synthetic models that do not rely on contact latches that are prone to wear. These discoveries set the stage for novel synthetic design and also enable empirical studies of latching dynamics in the many organisms with internal latches that cannot be visualized in vivo (1, 61–65).

Analysis of the dynamics of the proposed linkage model reveals that more elastic energy can be stored by shortening the joint-to-tendon link length (Fig. 4*A*). Therefore, the maximum energy storage can be directly controlled by allowing the joint-to-tendon link length to be varied (e.g., by using an additional actuator). Such a change to the linkage and actuation design would add additional degrees of freedom, similar to recent work on dynamics in biological systems (i.e., the four-bar opercular mechanism of largemouth bass) (66, 67).

As our analytical and physical models are similar in size to a mantis shrimp, a design optimization framework, based on these models, can be used as a tool in future investigations into the evolution of the mantis shrimp raptorial appendage (28, 46, 47, 49). These models can be matched to the morphologies found in the fossil record and evaluated using the proposed performance metrics to paint a picture of the trade-offs and adaptations over time. Similarly, the models could be used to optimize geometric linkage mechanisms and energy storage designs for high-performance robots. In this paper we aimed to emulate the dynamic properties of a mantis shrimp. However, the same linkage mechanism and analysis could be applied to other behaviors—for example, throwing or jumping—in which high power is required, albeit with different appendage trajectories. In particular, a direct application of our model is in the optimization of the latch geometric parameters (e.g., link lengths and the inclusion of additional linkage attachments on the arm) and spring/actuator designs to create a jumping robot at smaller scales and higher jumping velocities than previous examples. In addition, the high power amplification mediated by the linkage mechanism could further explain the role of feedback control in biological impulsive systems in future efforts (68).

Materials and Methods

Fabrication. To create a small-scale, robust mechanism, we use a lamination-and-folding fabrication process called pop-up book MEMS (59, 60), which enables the creation of articulated mechanisms with feature sizes ranging from micrometers to several centimeters. An UV laser (Oxford E series) is used to cut individual layers of carbon fiber composite, acrylic adhesive, and Kevlar/Kapton composite.

To construct the robot, a layup composed of rigid layers surrounding the flexure material and bonded with adhesive layers is aligned in a press and laminated under heat and pressure. The laminate structure is then released by a final laser cutting step. Gaps in the rigid layers that form the static and dynamic flexure hinges are highlighted in yellow in Fig. 1*C*. Static hinges are folded during assembly to form 3D structures which are fixed in place using a cyanoacrylate (CA) glue. The dynamic hinges act as the articulated joints of the device.

The fully assembled device is mounted to a 3D printed base. A rigid rod is glued in place through the robot body, and additional rods are inserted through the base to interface with the torsion springs. A Kevlar tendon is tied around a hole in the robot arm and threaded through holes in the base. The initial angle of the tendon can be adjusted by changing which hole it is passed through, as seen in Fig. 1*C*.

Motion Control and Capture. Experiments were conducted on the robot using the experimental setup depicted in *SI Appendix*, Fig. S3. The robot is actuated remotely with a Thor Labs K-Cube KDC101 controller and MTS25/M-Z8 motorized translation stage mounted in a vertical orientation. A Futek IAA100 amplifier and Futek LSB302 25lb load cell, mounted to the stage, measure the pulling force during the test. High-speed video is captured using a Vision Research Phantom v7.3. Frame rates up to 37,000 frames per second were used during testing. A National Instruments USB-6363 DAQ was used for triggering and data collection. The actuator pulls the tendon at a constant velocity.

List of Controlled Experiments. Various experiments were conducted to understand the range of achievable performance (i.e., maximum arm rotation speed and energy distribution between the arm and the body) depending on different controlled conditions. Three categories of control parameters are considered.

1. Tendon control: the pulling velocity of the kevlar string shown in Fig. 1*B* is regulated by an external motor controller. Multiple experiments were performed at different pulling velocities from 0.5 m s^{-1} to 2.3 m s^{-1}.
2. Environment: experiments were conducted with two fluid loading conditions, air and water. In each loading condition, multiple tendon control experiments were performed.
3. Design: multiple tendon attachment points were considered by changing the joint-to-tendon length, L_0 in Fig. 2*A*, from 19 to 23 mm. Also, different contact angles varying from 0° to 11.4° were tested. In each geometry, multiple tendon control experiments were performed.

Representative videos of striking experiments ($L_0 = 23\,mm$) in air and water are shown in Movies S1–S3: two experiments with different loading, Movies S1 (air) and S2 (water), and one experiment with a different contact angle using a shim to offset the arm, Movie S3 (with a contact angle of 6.4°).

Kinetic Energy Ratio and Normalized Potential Energy. As phase IV starts when the spring is loaded to its maximum extent, the normalized potential energy, PE/PE_{max}, starts from unity and decreases as the spring releases its energy in Fig. 5*D*. Also, at the beginning of phase IV, the body kinetic energy

becomes zero as the body is linked to the spring directly, which makes the arm kinetic energy ratio, KE_2/KE, also start from unity.

Controlled Experiments in Water. Eleven experiments in water were controlled such that the mean tendon velocities (trial to trial) and associated SDs stay similar to the mean and SDs in the air experiments. The mean tendon velocity among 11 experiments in water was 1.43 mm s^{-1} (0.73 mm s^{-1} SD) where the mean in air was 1.43 mm s^{-1} (0.79 mm s^{-1} SD).

Hydrodynamic Effects in Water. The higher accelerations of the robot during phases III and IV induce an added mass effect, resulting in increased kinetic energy due to the fluid entrained by the motion of the arm and body, adding to the effective inertia. Therefore, the added kinetic energy at the arm and the body are considered separately and included in the calculation of the kinetic energy ratio (*SI Appendix, Added-Mass Effect*).

Controlled Experiments in Air with Smaller Joint-to-Tendon Lengths. First, two distances for L_0 were chosen, 19 and 23 mm, and an additional 10 tendon velocity control experiments (in air) are conducted for the 19 mm case. Similar to the experiments in water, the tendon pulling velocity was controlled such that the mean pulling velocities (trial to trial) and associated SDs stay similar to the mean and SDs for experiments in air with $L_0 = 23$ mm. The mean tendon pulling velocities for each group are 1.32 mm s^{-1} (for 19 mm) and 1.43 mm s^{-1} (for 23 mm). The SDs for each group are 0.78 mm s^{-1} (for 19 mm) and 0.79 mm s^{-1} (for 23 mm).

The mean maximum tip velocity for both cases stays within 0.7% of 25.6 m s^{-1}, but the SD for the 19 mm case (0.96 m s^{-1}) is relatively smaller than the SD for the 23 mm case (2.04 m s^{-1}), up to the numerical precision of the postprocessing methods used (*Data Processing*).

Controlled Experiments in Air with Different Contact Angles. Seven tests with a set of fixed contact angles were performed to analyze the sensitivity of the performance metrics to changes in contact angle. The tendon pull velocities were regulated to 2.3 mm s^{-1} for all experiments. Two shims with different thicknesses were attached on the side of the body which comes in contact with the arm, offsetting the contact angle in proportion to the thickness of the shim: 0.0° (i.e., no shim), 6.4°, and 11.4°. See Movie S3 for the experiment with a 6.4° contact angle.

Motion Tracking. The 2D kinematic motion of our physical model is measured using ProAnalyst software (Xcitex). Template-matching object tracking is performed using high-contrast markers placed on the exterior of the robot at precise, known locations. The position of each marker is automatically tracked and recorded for each test. Further analysis is completed using a custom MATLAB optimization program.

Data Processing. The output from the motion tracking software provides the (x, y) position of tracking points in the camera frame. To compensate for quantization noise, a noncausal (zero phase) moving average filter with a variable window size is applied to the marker position data (*SI Appendix*, Fig. S10*A*). Data points in the slow moving prestrike portion of the data are smoothed using a larger window size while the fast moving striking data are filtered using a smaller window size. The filtered data are made continuous with a buffer region of linearly decreasing window size to the smaller window size used for fast movement.

First, the body pivot location (which stays constant throughout each experiment) is approximated based on the filtered tracking points. As the body rotates around the fixed pivot, the tracking points on the body will follow an arc. Therefore, an optimization problem is set up to find an arc for each marker which minimizes the distance (L2 norm) from the arc to the data points. The optimal solution returns the body pivot position in the camera frame. Next, the angular position of the body markers on the body is optimized by preserving the distance between the two markers fixed in position relative to each other. This optimized angular position of the marker, plus some offset, becomes the θ_1 dataset. An example of this fitting is shown in *SI Appendix*, Fig. S10*B*, where the identified θ_1 data are shown in *SI Appendix*, Fig. S10*C*.

On the other hand, the markers on the arm are known to pivot around a fixed body location. Therefore, another optimization process to find an arc from the floating arm pivot position estimates the arm pivot location in the camera frame. Last, the angular position of the arm with respect to the body frame is found by preserving the distance between the two markers, similar to the method used for the body, which produces the θ_2 dataset. An example of the floating arm pivot position is shown in *SI Appendix*, Fig. S10*D*, where the identified θ_2 is shown in *SI Appendix*, Fig. S10*E*.

This four-stage process, respecting known kinematics, provides more physically informed processed data compared to a simple frequency-based filtering technique. A detailed explanation can be found in section *SI Appendix, Optimization Based Data Processing*.

Data Availability. Kinematic data of the physical model analyzed in this paper have been deposited in GitHub, https://github.com/harvard-microrobotics/mantis-shrimp. Previously published data were used for this work (mantis shrimp strike data from ref. 33).

ACKNOWLEDGMENTS. We thank Yongjin Kim for the Kapton–Kevlar composite and Patrick Varin for his help early on with dynamic modeling. This material is based upon work supported by, or in part by, the US Army Research Laboratory and the US Army Research Office under contract/grant W911NF1510358.

1. W. Gronenberg, Fast actions in small animals: Springs and click mechanisms. *J. Comp. Physiol. A Neuroethol. Sens. Neural Behav. Physiol.* **178**, 727–734 (1996).
2. A. Galantis, R. C. Woledge, The theoretical limits to the power output of a muscle-tendon complex with inertial and gravitational loads. *Proc. Biol. Sci.* **270**, 1493–1498 (2003).
3. S. N. Patek, D. M. Dudek, M. V. Rosario, From bouncy legs to poisoned arrows: Elastic movements in invertebrates. *J. Exp. Biol.* **214**, 1973–1980 (2011).
4. M. Mark Ilton *et al*., The principles of cascading power limits in small, fast biological and engineered systems. *Science* **360**, eaao1082 (2018).
5. S. J. Longo *et al*., Beyond power amplification: Latch-mediated spring actuation is an emerging framework for the study of diverse elastic systems. *J. Exp. Biol.* **222**, 1–10 (2019).
6. S. Vogel, Living in a physical world II. The bio-ballistics of small projectiles. *J. Biosci.* **30**, 167–175 (2005).
7. S. Vogel, Living in a physical world III. Getting up to speed. *J. Biosci.* **30**, 303–312 (2005).
8. A. Sakes *et al*., Shooting mechanisms in nature: A systematic review. *PLoS One* **11**, e0158277 (2016).
9. M. V. Rosario, G. P. Sutton, S. N. Patek, G. S. Sawicki, Muscle–spring dynamics in time-limited, elastic movements. *Proc. R. Soc. B: Biol. Sci.*, **283**, 20161561 (2016).
10. S. M. Mark Ilton *et al*., The effect of size-scale on the kinematics of elastic energy release. *Soft Matter* **15**, 9579–9586 (2019).
11. P. Gregory *et al*., Why do large animals never actuate their jumps with latch-mediated springs? Because they can jump higher without them. *Integr. Comp. Biol.* **59**, 1609–1618 (2019).
12. O. Bolmin *et al*., Latching of the click beetle (Coleoptera: Elateridae) thoracic hinge enabled by the morphology and mechanics of conformal structures. *J. Exp. Biol.* **222**, jeb196683 (2019).
13. S. Divi, X. Ma *et al*., Latch-based control of energy output in spring actuated systems. *J. R. Soc. Interface* **17**, 20200070 (2020).
14. B. Webb, Using robots to model animals: A cricket test. *Robot. Auton. Syst.* **16**, 117–134 (1995).
15. K. Dianna *et al*., Addressing grand challenges in organismal biology: The need for synthesis. *Bioscience* **64**, 1178–1187 (2014).
16. D. L. Hu, M. Prakash, B. Chan, J. W. M. Bush, Water-walking devices. *Exp. Fluids* **43**, 769–778 (2007).
17. R. Altendorfer *et al*., Rhex: A biologically inspired hexapod runner. *Auton. Robots* **11**, 207–213 (2001).
18. F. Berlinger, J. Dusek, M. Gauci, R. Nagpal, Robust maneuverability of a miniature, low-cost underwater robot using multiple fin actuation. *IEEE Robot. Autom. Lett.* **3**, 140–147 (2017).
19. M. J. McHenry *et al*., The comparative hydrodynamics of rapid rotation by predatory appendages. *J. Exp. Biol.* **219**, 3399–3411 (2016).
20. S. N. Patek, W. L. Korff, R. L. Caldwell, Biomechanics: Deadly strike mechanism of a mantis shrimp. *Nature* **428**, 819–820 (2004).
21. S. N. Patek, R. L. Caldwell, Extreme impact and cavitation forces of a biological hammer: Strike forces of the peacock mantis shrimp *Odontodactylus scyllarus*. *J. Exp. Biol.* **208**, 3655–3664 (2005).
22. R. L. Crane, S. M. Cox, S. A. Kisare, S. N. Patek, Smashing mantis shrimp strategically impact shells. *J. Exp. Biol.* **221**, jeb176099 (2018).
23. T. I. Zack, T. Claverie, S. N. Patek, Elastic energy storage in the mantis shrimp's fast predatory strike. *J. Exp. Biol.* **212**, 4002–4009 (2009).
24. S. N. Patek, M. V. Rosario, J. R. A. Taylor, Comparative spring mechanics in mantis shrimp. *J. Exp. Biol.* **216**, 1317–1329 (2013).
25. M. V. Rosario, S. N. Patek, Multilevel analysis of elastic morphology: The mantis shrimp's spring. *J. Morphol.* **276**, 1123–1135 (2015).
26. M. Tadayon, S. Amini, A. Masic, A. Miserez, The mantis shrimp saddle: A biological spring combining stiffness and flexibility. *Adv. Funct. Mater.* **25**, 6437–6447 (2015).
27. M. Tadayon, S. Amini, Z. Wang, A. Miserez, Biomechanical design of the mantis shrimp saddle: A biomineralized spring used for rapid raptorial strikes. *iScience* **8**, 271–282 (2018).

28. S. N. Patek, B. N. Nowroozi, J. E. Baio, R. L. Caldwell, A. P. Summers, Linkage mechanics and power amplification of the mantis shrimp's strike. *J. Exp. Biol.* **210**, 3677–3688 (2007).
29. M. J. McHenry, T. Claverie, M. V. Rosario, S. N. Patek, Gearing for speed slows the predatory strike of a mantis shrimp. *J. Exp. Biol.* **215**, 1231–1245 (2012).
30. M. Burrows, The mechanics and neural control of the prey capture strike in the mantid shrimps squilla and hemisquilla. *Z. Vgl. Physiol.* **62**, 361–381 (1969).
31. M. Burrows, G. Hoyle, Neuromuscular physiology of the strike mechanism of the mantis shrimp, hemisquilla. *J. Exp. Zool.* **179**, 379–393 (1972).
32. M. S. deVries, E. A. K. Murphy, S. N. Patek, Strike mechanics of an ambush predator: The spearing mantis shrimp. *J. Exp. Biol.* **215**, 4374–4384 (2012).
33. K. Kagaya, S. N. Patek, Feed-forward motor control of ultrafast, ballistic movements. *J. Exp. Biol.* **219**, 319–333 (2016).
34. S. N. Patek, The power of mantis shrimp strikes: Interdisciplinary impacts of an extreme cascade of energy release. *Integr. Comp. Biol.* **59**, 1573–1585 (2019).
35. S. M. Cox, D. Schmidt, Y. Modarres-Sadeghi, S. N. Patek, A physical model of the extreme mantis shrimp strike: Kinematics and cavitation of Ninjabot. *Bioinspir. Biomim.* **9**, 016014 (2014).
36. S. J. Longo, T. Goodearly, P. C. Wainwright. Extremely fast feeding strikes are powered by elastic recoil in a seahorse relative, the snipefish, *Macroramphosus scolopax*. *Proc. R. Soc. B: Biol. Sci.* **285**, 20181078 (2018).
37. D. Cofer, G. Cymbalyuk, W. J. Heitler, D. H. Edwards, Neuromechanical simulation of the locust jump. *J. Exp. Biol.* **213**, 1060–1068 (2010).
38. T. Kaji, A. Anker, C. S. Wirkner, A. R. Palmer, Parallel saltational evolution of ultrafast movements in snapping shrimp claws. *Curr. Biol.* **28**, 106–113.e4 (2018).
39. S. N. Patek, S. J. Longo, Evolutionary biomechanics: The pathway to power in snapping shrimp. *Curr. Biol.* **28**, R115–R117 (2018).
40. J. A. C. Knowles, M. H. Lowenberg, S. A. Neild, B. Krauskopf, A bifurcation study to guide the design of a landing gear with a combined uplock/downlock mechanism. *Proc. R. Soc. Math. Phys. Eng. Sci.* **470**, 20140332 (2014).
41. J. A. C. Knowles, B. Krauskopf, M. H. Lowenberg, Numerical continuation applied to landing gear mechanism analysis. *J. Aircr.* **48**, 1254–1262 (2011).
42. H. C. Bennet-Clark, E. C. A. Lucey, The jump of the flea: A study of the energetics and a model of the mechanism. *J. Exp. Biol.* **47**, 59–67 (1967).
43. M. Noh, S.-W. Kim, S. An, J.-S. Koh, K.-J. Cho, Flea-inspired catapult mechanism for miniature jumping robots. *IEEE Trans. Robot.* **28**, 1007–1018 (2012).
44. J.-S. Koh *et al*., Jumping on water: Surface tension–dominated jumping of water striders and robotic insects. *Science* **349**, 517–521 (2015).
45. J.-S. Koh, J. Sun-pil, R. J. Wood, K.-J. Cho. "A jumping robotic insect based on a torque reversal catapult mechanism" in *2013 IEEE/RSJ International Conference on Intelligent Robots and Systems* (IEEE, 2013), pp. 3796–3801.
46. P. S. L. Anderson, T. Claverie, S. N. Patek, Levers and linkages: Mechanical trade-offs in a power-amplified system. *Evolution* **68**, 1919–1933 (2014).
47. P. S. L. Anderson, S. N. Patek, Mechanical sensitivity reveals evolutionary dynamics of mechanical systems. *Proc. R. Soc. B: Biol. Sci.* **282**, 20143088 (2015).
48. Y. Hu, N. Nelson-Maney, P. S. L. Anderson, Common evolutionary trends underlie the four-bar linkage systems of sunfish and mantis shrimp. *Evolution* **71**, 1397–1405 (2017).
49. M. M. Munoz, P. S. L. Anderson, S. N. Patek, Mechanical sensitivity and the dynamics of evolutionary rate shifts in biomechanical systems. *Proc. R. Soc. B: Biol. Sci.*, **284**, 20162325 (2017).
50. M. Muller, Optimization principles applied to the mechanism of neurocranium levation and mouth bottom depression in bony fishes (halecostomi). *J. Theor. Biol.* **126**, 343–368 (1987).
51. M. W. Westneat, Feeding mechanics of teleost fishes (Labridae; Perciformes): A test of four-bar linkage models. *J. Morphol.* **205**, 269–295 (1990).
52. M. W. Westneat, Transmission of force and velocity in the feeding mechanisms of labrid fishes (teleostei, perciformes). *Zoomorphology* **114**, 103–118 (1994).
53. M. Burrows, O. Morris, Jumping and kicking in bush crickets. *J. Exp. Biol.* **206**, 1035–1049 (2003).
54. T. J. Roberts, E. Azizi, Flexible mechanisms: The diverse roles of biological springs in vertebrate movement. *J. Exp. Biol.* **214**, 353–361 (2011).
55. R. M. Murray, Z. Li, S. Sastry, *A Mathematical Introduction to Robotic Manipulation* (CRC Press, 2017).
56. J. P. Whitney, P. S. Sreetharan, K. Y. Ma, R. J. Wood, Pop-up book mems. *J. Micromech. Microeng.* **21**, 115021 (2011).
57. P. S. Sreetharan, J. P. Whitney, M. D. Strauss, R. J. Wood, Monolithic fabrication of millimeter-scale machines. *J. Micromech. Microeng.* **22**, 055027 (2012).
58. J. M. Birch, M. H. Dickinson, Spanwise flow and the attachment of the leading-edge vortex on insect wings. *Nature* **412**, 729–733 (2001).
59. C. Li, S. T. Hsieh, D. I. Goldman, Multi-functional foot use during running in the zebra-tailed lizard (*Callisaurus draconoides*). *J. Exp. Biol.* **215**, 3293–3308 (2012).
60. D. P. Holmes, A. J. Crosby, Snapping surfaces. *Adv. Mater.* **19**, 3589–3593 (2007).
61. H. C. Astley, T. J. Roberts, Evidence for a vertebrate catapult: Elastic energy storage in the plantaris tendon during frog jumping. *Biol. Lett.* **8**, 386–389 (2012).
62. H. C. Astley, T. J. Roberts, The mechanics of elastic loading and recoil in anuran jumping. *J. Exp. Biol.* **217**, 4372–4378 (2014).
63. F. J. Larabee, A. V. Suarez, The evolution and functional morphology of trap-jaw ants (hymenoptera: Formicidae). *Myrmecol. News* **20**, 25–36 (2014).
64. R. Ritzmann, Snapping behavior of the shrimp *Alpheus californiensis*. *Science* **181**, 459–460 (1973).
65. E. R. Ritzmann, Mechanisms for the snapping behavior of two alpheid shrimp, *Alpheus californiensis* and *Alpheus heterochelis*. *J. Comp. Physiol.* **95**, 217–236 (1974).
66. A. M. Olsen, A mobility-based classification of closed kinematic chains in biomechanics and implications for motor control. *J. Exp. Biol.* **222**, jeb195735 (2019).
67. A. M. Olsen, A. L. Camp, E. L. Brainerd, The opercular mouth-opening mechanism of largemouth bass functions as a 3d four-bar linkage with three degrees of freedom. *J. Exp. Biol.* **220**, 4612–4623 (2017).
68. N. J. Cowan *et al*., Feedback control as a framework for understanding tradeoffs in biology. *Integr. Comp. Biol.* **54**, 223–237 (2014).
69. J.-S. Koh, S.-P. Jung, M. Noh, S.-W. Kim, K.-J. Cho, "Flea inspired catapult mechanism with active energy storage and release for small scale jumping robot " in *2013 IEEE International Conference on Robotics and Automation* (IEEE, 2013), pp. 26–31.
70. G. P. Sutton, M. Burrows, Biomechanics of jumping in the flea. *J. Exp. Biol.* **214**, 836–847 (2011).
71. T. Ayling, *Guide to the Sea Fishes of New Zealand* (William Collins Publishers Ltd, Auckland, New Zealand, 1982).
72. P. A. Green, S. N. Patek, Contests with deadly weapons: Telson sparring in mantis shrimp (Stomatopoda). *Biol. Lett.* **11**, 20150558 (2015).